University of Groningen

Encounters between spherical galaxies - II. Systems with a dark halo

Gonzalez-Garcia, A. C.; van Albada, T. S.

Encounters between spherical galaxies – II. Systems with a dark halo

A. C. González-García[1,2]★ and T. S. van Albada[1]

[1]*Kapteyn Astronomical Institute, PO Box 800, 9700 AV Groningen, the Netherlands*
[2]*Instituto de Astrofísica de Canarias, Vía Láctea s/n, La Laguna, 38200, Spain*

ABSTRACT

We perform *N*-body simulations of encounters between spherical systems surrounded by a spherical halo. Following a preceding paper with a similar aim, the initial systems include a spherical Jaffe model for the luminous matter and a Hernquist model for the halo. The merger remnants from this sample are mainly slowly rotating, prolate spheroids with a radially anisotropic velocity distribution. The results are compared with real-life ellipticals and with the models without halo in Paper I. We argue that elliptical galaxies with evidence of dark matter could be formed in the field via a merger of spheroids surrounded by a dark matter halo, while ellipticals with no evidence of dark matter might be formed via a merger of two spheroids in a cluster.

Key words: methods: *N*-body simulations – galaxies: interactions – galaxies: kinematics and dynamics – galaxies: structure – elliptical.

1 INTRODUCTION

In the preceding paper (González-García & van Albada 2005, hereafter Paper I), encounters of one-component spherical isotropic systems were studied. Several initial conditions were investigated systematically in order to link the end products of the simulations with real-life elliptical galaxies. Both mergers and non-mergers were produced and analysed. From that study we conclude that various properties of elliptical galaxies can be explained by interactions between spheroids. In particular, ellipticity, rotation and boxiness–disciness can be attributed to the initial amount of angular momentum in the collision orbit. The mass ratio of the progenitor galaxies and the orbital energy mainly affect the final outcome of the interaction (i.e. whether it is a merger or not) and the morphology of the merger remnant.

In the present paper, we study how these results are modified when a dark halo is present.

The amount of dark matter in elliptical galaxies is still controversial. The lack of H I in elliptical galaxies complicates this issue, and a number of alternative ways have been proposed to study the amount of dark matter (cf. gravitational lensing: Keeton, Kochanek & Falco 1998; X-ray haloes: Matsushita et al. 1998; planetary nebula: Romanowsky et al. 2001; stellar kinematics: Saglia, Bertin & Stiavelli 1992; Kronawitter et al. 2000). These studies show that there is evidence for the presence of dark haloes, although dark matter does not seem to be important in the inner ($R < R_e$) parts of elliptical galaxies.

Saglia, Bender & Dressler (1993), and more recently Napolitano et al. (2005), argue that possibly two populations of ellipti-

cals exist. One would be dark matter dominated while in the other a diffuse halo, or perhaps no dark matter at all, would be present.

Traditionally, merger simulations involving a dark matter component have dealt with mergers between disc galaxies (see Barnes 1998, for a review). Simulations involving spherical systems do not usually deal with two-component models (for a review see Paper I). In recent years some effort has been devoted to modelling such encounters with the purpose of studying the Fundamental Plane of elliptical galaxies (Dantas et al. 2003; González-García 2003, chapter 5), but little attention has been given to the characteristics of the remnant of those encounters.

In the present paper, we study a sample of merger simulations of spherical systems embedded in a halo. These simulations do not intend to cover the entire initial parameter space. Rather, they aim at a comparison with the no-halo merger remnants of Paper I and with observations.

2 MODELS

2.1 Initial conditions

In constructing the initial systems, we follow the same strategy as in Paper I, i.e. we use Jeans' theorem and Eddington's formula to relate the distribution function (DF) to the potential of our systems.

The systems include a luminous bulge, representing the distribution of light in elliptical galaxies, and a dark matter halo. We use the Jaffe (1983) sphere used in Paper I, to model the luminous matter, and a Hernquist (1990a) sphere for the dark halo. Jaffe and Hernquist models are two examples of potential–density pairs with an analytical solution for the DF. In fact, they are part of a larger family of models studied by Dehnen (1993).

★E-mail: Cesar.gonzalez@iac.es

The relevant quantities are the following. The potential for a Jaffe model is

$$\phi_L(r) = \frac{GM_L}{r_J} \ln\left(\frac{r}{r + r_J}\right), \tag{1}$$

where G is Newton's constant of gravity, M_L is the luminous mass of the system and r_J is the half-mass radius of the luminous component. The corresponding mass density is

$$\rho_L(r) = \left(\frac{M_L}{4\pi r_J^3}\right) \frac{r_J^4}{r^2(r + r_J)^2}. \tag{2}$$

The potential of the Hernquist model is

$$\phi_H(r) = -\frac{GM_H}{r + a}, \tag{3}$$

where M_H is the mass of the halo and a is the scalelength. The corresponding mass density is

$$\rho_H(r) = \left(\frac{M_H}{2\pi r}\right) \frac{a}{(r + a)^3}. \tag{4}$$

The half-mass radius of the dark halo component is equal to $(1 + \sqrt{2})a$. Combining a Jaffe model with a Hernquist model, we have a two-parameter family that depends on the ratio between the masses of the two systems M_L/M_H and the ratio between the half-mass radii:

$$r_{L1/2}/r_{H1/2} = \frac{r_J}{(1 + \sqrt{2})a}. \tag{5}$$

To find the DF for the two components separately, Eddington's formula (Binney & Tremaine 1987; equation 4–140b) has to be solved for the different densities in the potential generated by the total density, with

$$\rho_T = \rho_L + \rho_H, \tag{6}$$

$$\phi_T = \phi_L + \phi_H. \tag{7}$$

Then the DF of the combined system is

$$f_T(E) = f_L(E) + f_H(E). \tag{8}$$

An algorithm yielding $f_L(E)$ and $f_H(E)$ along the two-parameter family was developed by Smulders & Balcells (1995). The models used here were constructed using that algorithm.

We took our systems to be spherical and non-rotating, with an isotropic velocity distribution. In this regard, they are similar to the set of spherical isotropic systems without halo studied in Paper I.

In our models we have tried a range of M_H/M_L values, and calculated the circular velocity curve for those realizations (bearing in mind that we use a Jaffe–Hernquist model) and aiming at a flat-topped curve for a significant radial range. After several trials, we came to the conclusion that for the model with total mass $M_T = 1$ a value of $M_H/M_L = 9$ and a halo scalelength $a = 2$ (for $r_J = 1$) was the best choice for our purposes (see Fig. 1). A further scaling of this mass ratio was done following a scheme presented below (Section 2.5).

A cut-off radius has been imposed on the numerical implementation of this two-component model. The cut-off radius is equal to $10 \times r_J$. The theoretical and experimental values of the half-mass radius are then no longer equal. A distinction between r_J and a (theoretical values) and $r_{L1/2}$ and $r_{H1/2}$ (computational values) will therefore be made.
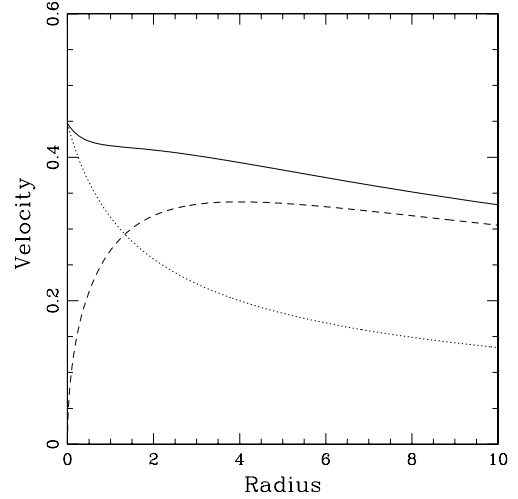

Figure 1. Circular velocity curves for the initial model. Parameters were chosen such that the circular velocity curve (top curve) is approximately flat. The dotted curve refers to the contribution by the Jaffe model and the dashed line to the Hernquist model.

2.2 Units

The results in this paper are presented in non-dimensional units such that Newton's constant of gravity $G = 1$, and the theoretical half-mass radius, r_J, for the Jaffe model is also equal to 1. Finally, the total mass of the initial system is also equal to unity. A possible set of units to scale our models to values for real galaxies, and allowing a comparison with observations, would be

$$[M] = 10^{12} \, M_\odot, \tag{9}$$

$$[L] = r_J = 5 \, \text{kpc}, \tag{10}$$

$$[T] = 5.27 \times 10^7 \, \text{yr}. \tag{11}$$

With these, the unit for velocity is

$$[v] = 1000 \, \text{km s}^{-1}. \tag{12}$$

2.3 Method

As in Paper I, we used Hernquist's (1987, 1990b) version of the TREECODE on an Ultra-Sparc station. Softening was set to 1/8 of the half-mass radius of the Jaffe core of the smallest galaxy ($r_{L1/2} = 0.82$ and $\varepsilon = 0.1$), the tolerance parameter was set to $\theta = 0.8$, quadrupole terms were included in the force calculation and the time step was set to 1/100 of the half-mass crossing time. We have used variable time steps, allowing refined calculations depending on the particle density. A typical run takes of the order of 5×10^5 s.

2.4 Stability of initial systems

We have checked the stability of the various initial systems by letting them evolve for more than 10 crossing times of the smallest component (i.e. the Jaffe bulge in this case), and checking that the systems are stable at different radii. We do this for a system with 40 000 particles in Hernquist's halo and 10 000 in the Jaffe component.

Fig. 2 (top) shows that after some adjustment, the systems reach equilibrium. The expansion seen in the inner parts of the luminous
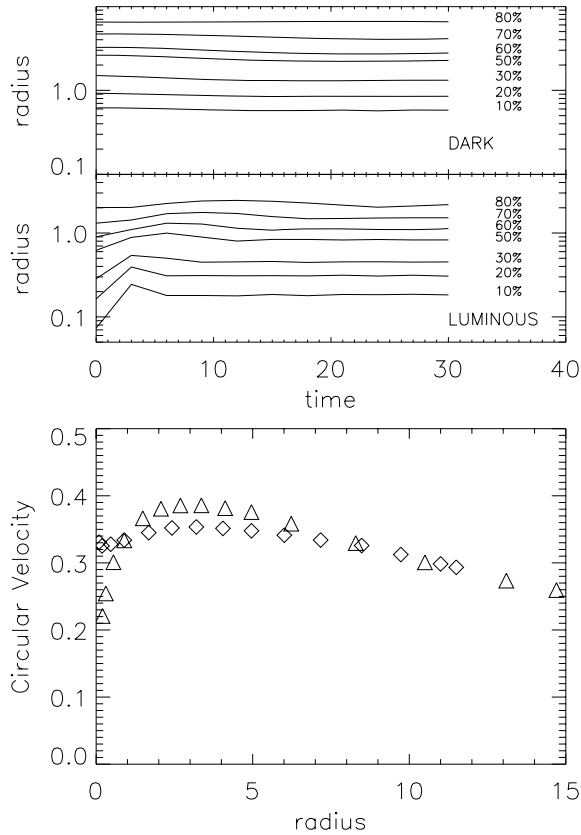
Table 1. Initial parameters for the progenitor models.

M_T	M_L	r_J	M_H	a
0.5	0.0574	0.7576	0.4426	1.4025
1	0.1	1	0.9	2
2	0.1741	1.3195	1.8259	2.8487

Figure 2. Top: Evolution of the radial mass distribution of the dark and luminous particles for our bulge-halo system with $M_T = 0.5$. After a mild reorganization of the luminous component, the system is in equilibrium. Bottom: Circular velocity curve for the initial system (diamonds) and the relaxed one (triangles).

component can probably be attributed to the softening introduced through the TREECODE in the force calculation. After this adjustment, the circular velocity curve is still approximately flat (Fig. 2, bottom).

2.5 Initial parameters

We construct three different initial configurations, with masses 1/2, 1 and 2.

We have scaled the *M/L* ratio inside these systems with the following assumptions. The total mass of the system is given by the combined mass of the dark matter halo and luminous component. For the luminous part (Jaffe bulge) we take *M/L* constant.

Further, we assume that our systems would initially lie on the observed Fundamental Plane so the *M/L* ratio of the combined system should follow a scaling law like $M/L \propto M^\alpha$ (Renzini & Ciotti 1993). Following Jørgensen, Franx & Kjærgaard (1996) we use

$$\log L \simeq 0.78 \log M + \text{constant}. \qquad (13)$$

The scaling of the masses and radii between different mass models is a bit more tricky than that in Paper I, because now we want the luminous matter to be scaled following a relation between mass and luminosity similar to that found via the Fundamental Plane (equation 13) and the relation between mass and radius for different

models given by Fish's (1964) law:

$$\frac{R_1}{R_2} = \sqrt{\frac{M_1}{M_2}}. \qquad (14)$$

Using equation (13) we scaled the relation between luminous and total matter as follows:

$$\frac{M_T^{4/5}}{M_L} = \text{constant}, \qquad (15)$$

and we use Fish's law (equation 14) to scale the radii of the two components for the systems of different mass. The parameters of the initial systems are given in Table 1.

We restrict ourselves to parabolic orbits, so $E_{\text{orb}} = 0$ for all our simulations. The impact parameters are chosen such that the encounters will lead to mergers.

To study the influence of orbital angular momentum on the merger remnant we have used three different impact parameters, head-on ($D = 0$), and two off-axis: one with D equal to half of the radius enclosing 99 per cent of the luminous mass of the bigger system, $D = r_L/2$, and one with D equal to that radius, $D = r_L$ (this radius corresponds to 95 per cent of the total, luminous+dark, mass).

The resulting mass ratios, orbital energies and impact parameters are given in Table 2. The model numbers reflect the mass ratio, and the type of orbit is indicated by a letter with *h* for head-on, *o* for offset and *g* for grazing encounters. This notation is similar to that used in Paper I, but now we do not include a letter for the orbital energy because it is always equal to zero.

In each simulation, the two galaxies were initially placed at a distance between their edges equal to the radius of the smallest galaxy. In the simulations without halo described in Paper I twice this radius was used. For more than half of this distance, tidal interaction was negligible however. To reduce computing time, we therefore decided to use a separation between the centres equal to $2R_1 + R_2$, where R_1 refers to the smallest system and R_2 to the largest.

Each galaxy has 50 000 particles, 40 000 particles in the Hernquist realization of the dark halo and 10 000 particles in the Jaffe luminous component.

Table 2. Input parameters for the merger simulations. The columns give the model name, the mass ratio, impact parameter and orbital energy.

Run	$M_2 : M_1$	Impact parameter	E_{orb}
1*h*	1:1	0	0
1*o*	1:1	5	0
1*g*	1:1	10	0
2*h*	2:1	0	0
2*o*	2:1	7.07	0
2*g*	2:1	14.14	0
4*h*	2:1/2	0	0
4*o*	2:1/2	7.07	0
4*g*	2:1/2	14.14	0

Table 3. Properties of the merger remnants. Columns give the model number (1), the time where the run was stopped (2), the line-of-sight ellipticity at R_e from a point of view perpendicual to the inital angular momentum vector (3), the axis ratios b/a (4), and c/a (5), and the ratio between the maximum rotational velocity and the central velocity dispersion (6).

Run (1)	t_{fin} (2)	ϵ (3)	b/a (4)	c/a (5)	V_{max}/σ_o (6)
1h	144	0.621	0.676	0.622	0.157
1o	150	0.530	0.684	0.644	0.262
1g	225	0.564	0.690	0.650	0.228
2h	200	0.593	0.702	0.669	0.175
2o	200	0.520	0.695	0.681	0.175
2g	360	0.573	0.772	0.695	0.456
4h	225	0.359	0.757	0.741	0.162
4o	250	0.265	0.807	0.756	0.173
4g	600	0.222	0.864	0.788	0.474

In the present runs, we have increased the total number of particles with respect to the simulations without halo by a factor of 5. The number of luminous particles, however, is kept low. We have proceeded in this manner due to the need to model live haloes with massive particles. If particles are too massive, particle–particle approaches are expected to heat the system if the difference in mass between particles is large. Models were let to evolve for at least 8–10 dynamical times of the merged system after merging to allow the system to relax (reach virialization). Conservation of energy is good in all the runs, better than 0.5 per cent.

3 RESULTS

The main characteristics of the merger remnants resulting from these encounters are summarized in Table 3. A short description of the relevant features is given below.

3.1 Phenomenology

Our models develop a variety of characteristics during the collision stages. Some examples are shown in Figs 3–5.

Fig. 3 is an example of a collision with mass ratio 1:1. The two galaxies are placed on a parabolic orbit with an impact parameter equal to half the outer radius of the luminous bulge. Around time 50 the systems meet for the fist time. After this first encounter both galaxies develop 'plumes'. A merger follows when the two galaxies meet for the second time, in an almost rectilinear orbit. Thus the final system is prolate. In Fig. 4 a pair with mass ratio 2:1 is shown. The impact parameter in this encounter is equal to the outer radius of the largest galaxy. The smaller galaxy (at the top in the first frame of Fig. 4) develops tails after the encounters around times 60 and 250. The final orbit, prior to the encounter, is less rectilinear than in the previous case. The final system is triaxial.

Finally, Fig. 5 shows a head-on collision for a run with mass ratio 4:1. The small galaxy (system at the top in the first frame of Fig. 5) suffers a reorganization of its particles in a system of shells after several passages through the potential well of its massive neighbour. The shells are visible in the final frames (see also Figs 9 and 10).

The general behaviour of these models is similar to that of the models without dark halo in Paper I. The main difference is in the sharpness of the shells that can be seen in models with a halo.

3.2 Morphology of the systems

In Figs 6–8, examples of the final states of different runs are shown. These illustrate the structural differences resulting from the variation in the orbital parameters. Each plot consists of two frames, the top one gives the distribution of halo particles, and the bottom one gives the distribution of luminous particles, both as seen along the z-axis, that is, the axis perpendicular to the orbital plane.

In Fig. 6 the remnant of run 1h is shown. This is a head-on parabolic collision, which is reflected in the symmetry of the remnant for both the dark and the luminous component. Some of the luminous particles in the 'plumes' have enough energy to escape from the potential well, but most will eventually fall back. Head-on collisions generally show a similar behaviour, with details depending on the masses of the progenitor systems. For non-equal mass collisions, this symmetry seen in Fig. 6 is broken. The smaller system will be highly disrupted giving rise to a one-sided lobe in the halo.

Head-on collisions without dark matter show a similar behaviour. The end products for equal mass models also show plumes surrounding the main prolate core. The potential there is shallower, however, and a larger number of particles will eventually escape (see Paper I).

Fig. 7 shows the particle configuration for model 2o. The initial (parabolic) orbit has a modest impact parameter. This is reflected in the end product via the prominent tails on both the dark (top panel) and the luminous (bottom) component. The larger one is coming from the progenitor of mass 1, which also presents small shells (see further below). Models with a moderate impact parameter usually merge after the second pass through the pericentre. Therefore, the merger remnant will have at least two or more tails, the precise number depending on the number of pericentre passages. The inner parts of the luminous component are nearly prolate.

The end product of encounters of one-component systems with parabolic orbits (Paper I) is, in general, a triaxial spheroid. It also shows some evidence of tails developed during the interaction stages, and the number of tail is again connected to the number of pericentre passages. So, we find that the behaviour is similar.

Fig. 8 illustrates the final state of run 4g. Here the parabolic orbit has a fairly large impact parameter. As a result, several tails in both components can be seen. Tails are mainly coming from the system with smallest mass at the beginning of the run. In the inner parts, we could also see prominent shells like those already mentioned for models 2o and 4h. As in those runs, these shells are formed from particles of the less massive system (see below). For simulations with a large impact parameter, the tails are more prominent than for small D, because the galaxies merge only after several passes through the pericentre. Particles in the tails will eventually fall back to the inner regions because they do not have enough energy to escape. Note, however, that the simulations were stopped when the material in the tails was still falling back. The overall shape of the system will not be affected appreciably by the returning material since the mass involved in the tails is small. Since this material carries most of the angular momentum, it may change the kinematics of the inner parts.

Again, similar structures can be seen in simulations involving a fair amount of angular momentum in the sample without dark halo of Paper I. Several tails are formed as a consequence of the interactions and the exchange of orbital angular momentum. These tails or plumes carry away a part of this angular momentum that will eventually return to the main body when the particles in those tails fall back to the main body.
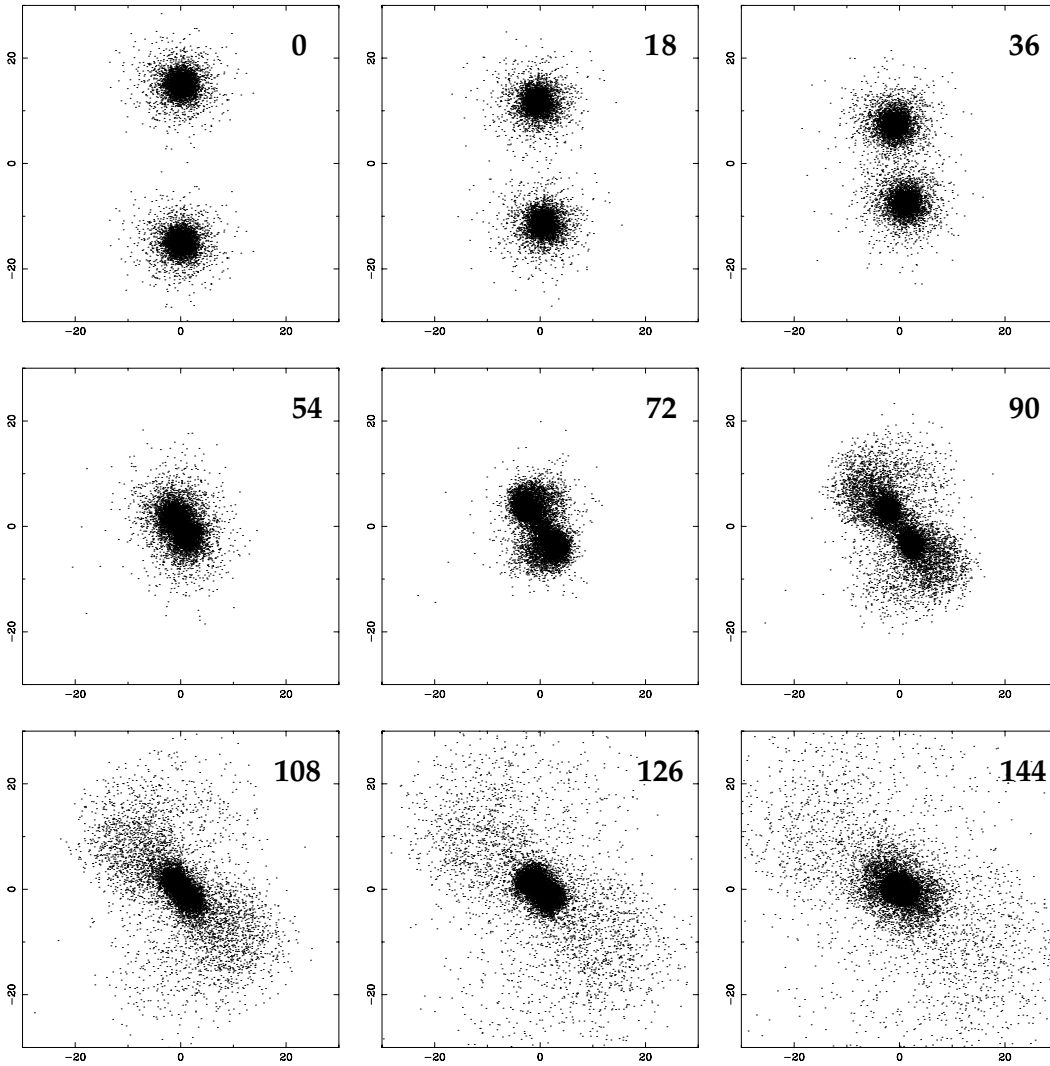
Figure 3. Evolution of systems in run 1*o*. This is a collision between two equal mass galaxies on a parabolic orbit with a small impact parameter. Only luminous particles are shown. Numbers at the top of each frame show the time in computational units. The first encounter occurs around time 50.

The dark haloes of the merger remnants have a variety of shapes depending on the initial conditions. For all our simulations, this shape is, grosso modo, the same as that of the luminous matter. Or, in other words, one can trace the shape of the dark matter using the luminous particles.

Head-on equal mass merger collisions result in a prolate structure of the final luminous components. As expected, these are symmetric due to the initial symmetry introduced by the choice of orbital parameters. Equal mass mergers in general do show a high degree of symmetry both in the luminous matter and in the dark matter. A similar symmetry results for head-on collisions with non-equal mass mergers about the line connecting the initial systems. This would be reflected in a small isophote twisting for these systems depending on the point of view.

The asymmetries present in non-equal mass off-axis mergers are more interesting. The smallest system is most affected by the encounter, forming prominent 'plumes' or tidal tails while the large system remains almost undisturbed. These systems would show prominent isophote twisting as well.

These results are in good agreement with those presented in Paper I for similar initial mass ratios and orbital parameters.

Shells are among the prominent features we find in the non-equal mass mergers in our sample. Fig. 9 shows the luminous particles of the small system in the final remnant of run 2*o*. We show two examples of radial velocity versus spherical radius plots in Fig. 10 for runs 2*o* and 4*h*. The first one is a parabolic encounter with a mild impact parameter. The shells look symmetric but are not very prominent. Run 4*h* is a head-on encounter where the particles of the small system end up in prominent shells.

As stated in section 3.2 in Paper I, shells are also formed there. However, the shells found in models with a dark mater halo are more prominent than those found there.

These features are summarized in Table 4 where a Hubble-type classification is given for the luminous part of the merger remnants. This classification is obtained after fitting the projected isodensity contours by ellipses for 100 random points of view. We have taken the mean projected ellipticity inside R_e (the radius enclosing half of the mass in projection). The classification given in Table 4 is the
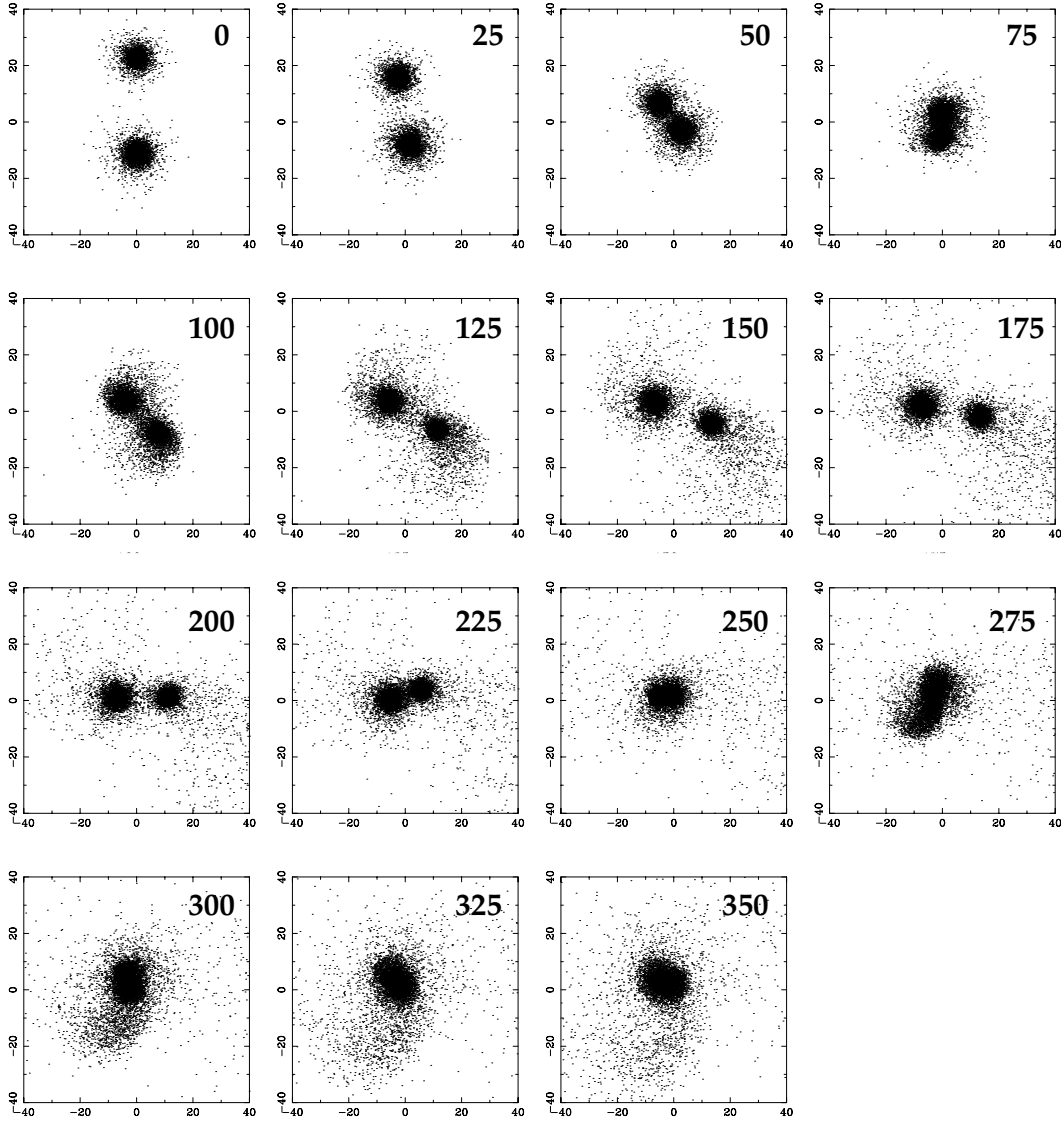
Figure 4. Evolution of systems in run 2*g*. This is a collision between two galaxies with mass ratio 2:1 on a parabolic orbit with an impact parameter equal to the outer radius of the luminous part of the large galaxy. Only luminous particles are shown. Numbers at the top of each frame show the time in computational units. The first encounter is around time 60. Tidal tails or 'plumes' form after the encounters, these consist mainly of material coming from the smallest system.

median of those ellipticities. (Note that in Table 3 we give the value ϵ of the ellipticity of the ellipse at R_e from the point perpendicular to the initial angular momentum vector). Also a description of the phenomenology in the halo and the luminous part of the remnant is given in Table 4.

3.3 Prolate and oblate systems

For each system, we have measured the axial ratios b/a and c/a, where a, b and c are the semi-axes of the luminous part, as calculated from the inertia tensor eigenvalues following the algorithm described in section 3.3 of Paper I. In these experiments with dark haloes, the luminous remnants are mainly prolate or triaxial spheroids. The results are shown in Fig. 11. We fail to find oblate spheroids, but our sample is too limited to reach a firm conclusion regarding shapes.

When we compare with fig. 10 in Paper I, in which the non-halo models are plotted, we note that in the simulations including haloes the final systems are more flattened than without halo. Values of c/a as small as 0.6 are found, whereas without halo the most extreme flattening is 0.7. However, there we did find oblate as well as triaxial and prolate spheroids.

Because the choice for the ratio between dark and luminous mass has been rather arbitrary, one may speculate whether even more flattened and oblate systems could be found with the appropriate set of parameters.

3.4 Rotation and flattening

For each of our merger remnants, we have fitted the projected isodensity contours by ellipses for 100 random points of view. Then we have measured the ellipticity for the luminous part inside the half
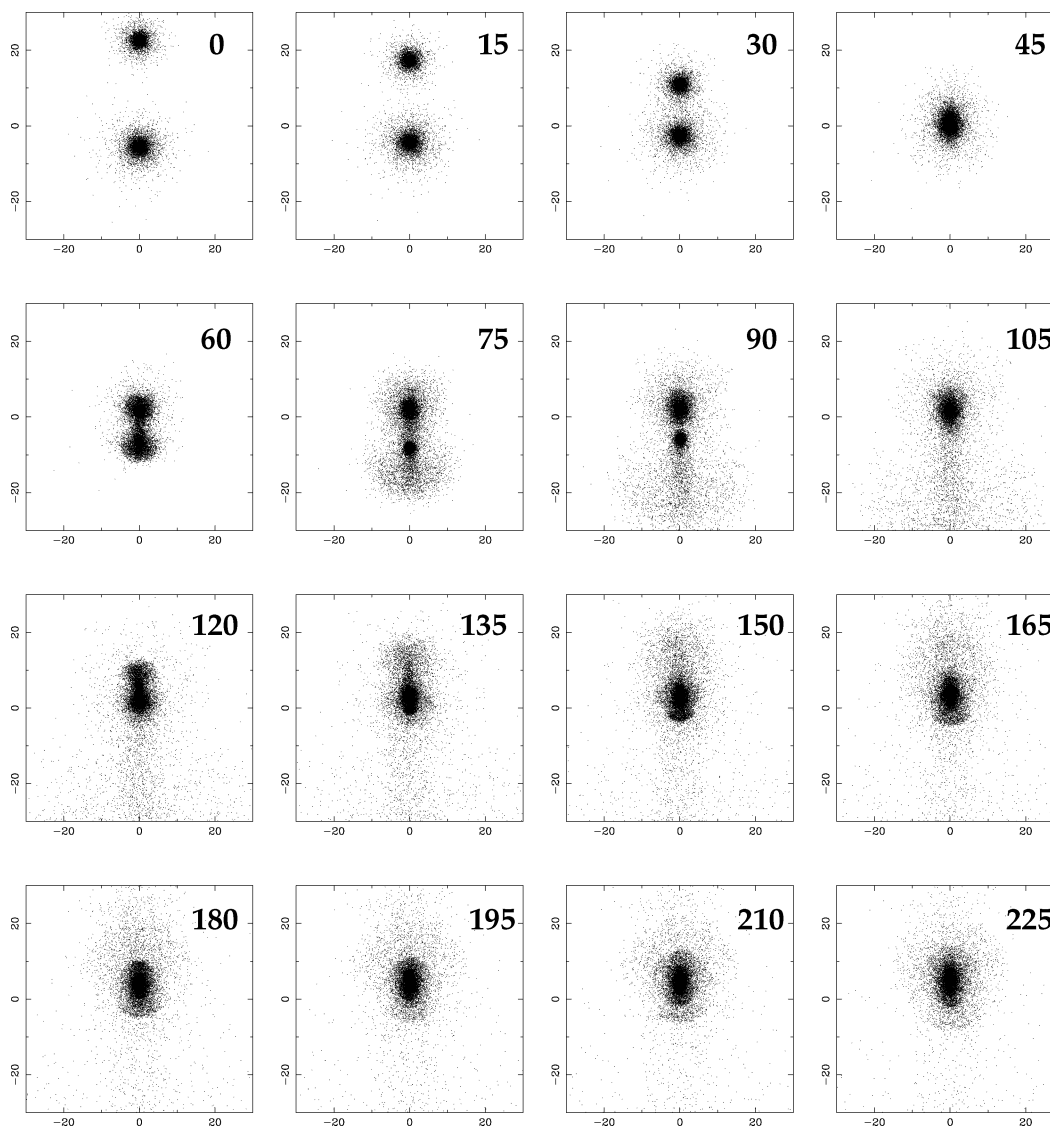
Figure 5. Evolution of systems in run 4*h*. This is a head-on collision between two galaxies with mass ratio 4:1. Only luminous particles are shown. Numbers at the top of each frame show the time in computational units. The first encounter occurs around time 40. The particles from the smallest system are redistributed after several passages through the largest one and end up in prominent shells.

luminous-mass radius. The mean of these results is shown in Fig. 12. The full range of morphological types, from E0 to E7, is covered. It may come as a surprise that E6/E7 systems are produced in collisionless *N*-body simulations. We have therefore checked this result by visual inspection of the isophote shapes in a number of cases. Although the isophotes are sometimes rather irregular, our visual inspection confirms the E6/E7 shape inside about one effective radius. Farther out, the isophotes often have a peanut shape. It appears that in these cases one is looking at the end result of a head-on collision from a point of view perpendicular to the relative orbit.

We find a peak at E3, as is observed in real-life ellipticals, although this is most probably accidental, given the restricted set of parameters used. As found in the simulations without dark halo, the runs in which the progenitors are of comparable mass result in higher ellipticities.

In Fig. 13, $V_{\max}/\sigma_\mathrm{o}$ is plotted versus ϵ. Over-plotted are observational data from Davies et al. (1983). We find that the models can cover most of the observed range. In general we see that the maximum rotation is not high. For a model with a large mass ratio (4:1), the merger process is still effective in forming a rotating system. When comparing this with fig. 11 in Paper I, we see that both samples are able to reproduce mildly rotating ellipticals. We find a difference, though, for the fast rotators. For non-halo models we find that models with a large amount of angular momentum lie close to the locus of the oblate rotators. For models with halo, we only find this for models with a large mass ratio and large angular momentum. However, we do not have flattened rotating oblate spheroids in the sample with dark halo.

These results indicate that the amount of dark matter (together with the orbital angular momentum and mass ratios, see Paper I)
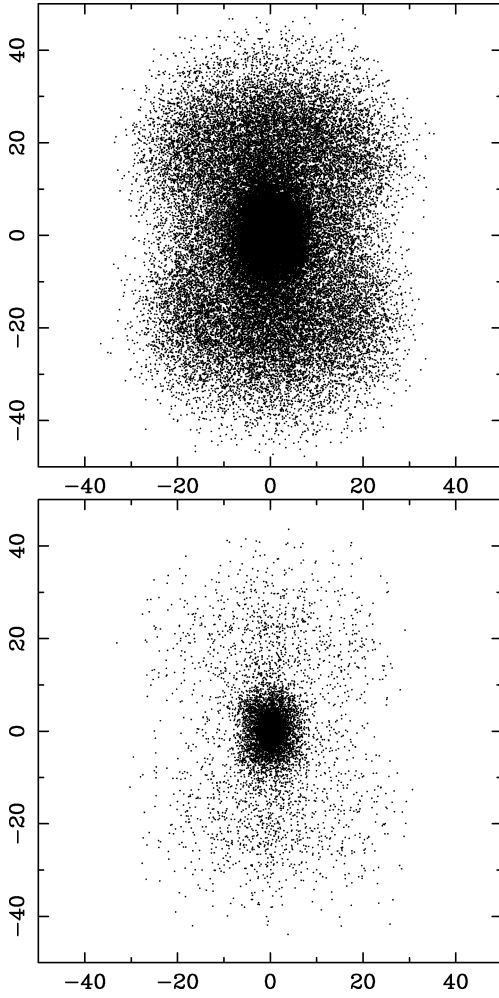
Figure 6. Particle distributions for halo (top) and luminous (bottom) components for run 1*h* as seen along the *z*-axis. This is a head-on collision in a parabolic orbit, which is reflected in the symmetry of the remnant. Some of the luminous particles in the plumes have enough energy to escape from the potential well, but most will fall back on the central system.

determines the amount of rotation, i.e. angular momentum, that is transferred to the luminous parts.

3.5 Boxiness–disciness

We have calculated the deviation from pure ellipses for our merger simulations.

When a deviation at a given isophotal level is discy, the a_4 parameter is positive, while for boxy deviations this parameter is negative (see Binney & Merrifield 1998, and section 3.5 in Paper I).

In Fig. 14 we present the deviations for model 1*g*. To increase the signal-to-noise ratio an average over 60 snapshots were made, always calculating the isophotes for a projection parallel to the intermediate-axis. These 60 snapshots are obtained by evolving the end products a bit further in time.

We find that a highly boxy system is formed. The remnant is boxy out to two effective radii. The large boxiness found here is in contrast with the modest boxiness found in the models without halo. Here we find that all systems are boxy while some of the systems in Paper I, using similar orbital parameters, are discy.
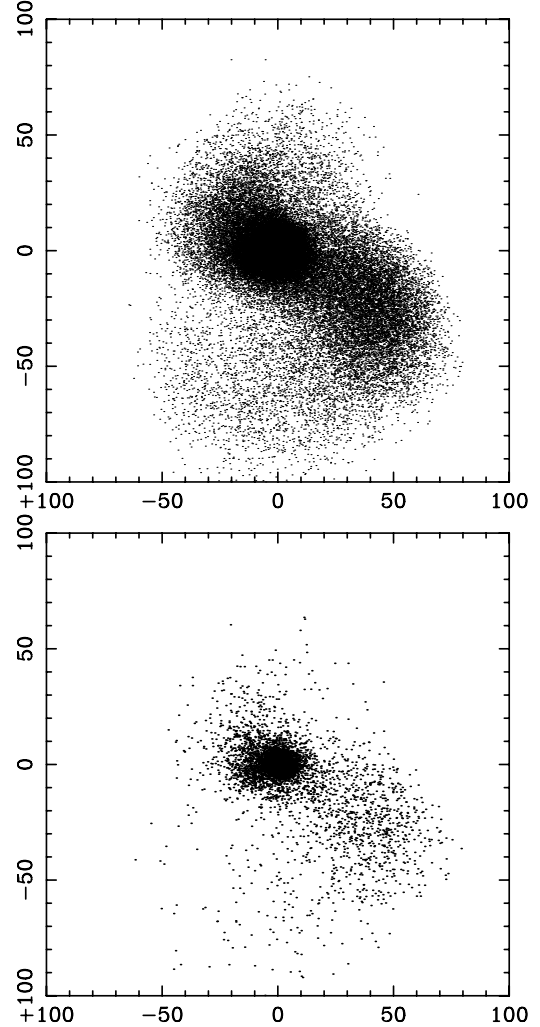

Figure 7. Particle distributions for halo (top) and luminous (bottom) components for run 2*o* as seen along the *z*-axis. The initial configuration of this run has a parabolic orbit with a moderate impact parameter. This is reflected in the end product via the prominent tails in both the dark and the luminous component. The large tail is coming from the progenitor of mass 1, i.e. the least massive galaxy.

3.6 Kinematics

For the models with haloes, we do not find such a clear rotation as found for non-halo mergers (see section 3.6 in Paper I). Only weak rotation is found in the cases with the highest impact parameter (larger angular momentum).

Elliptical galaxies are mainly supported by random motions. To measure the velocity anisotropy, we used the β parameter defined as

$$\beta = 1 - \frac{\sigma_t^2}{2\sigma_r^2}, \tag{16}$$

with σ_t the tangential velocity dispersion ($\sigma_t^2 = \sigma_\theta^2 + \sigma_\phi^2$) and σ_r the radial velocity dispersion (see section 3.6 in Paper I).

Fig. 15 shows how this parameter changes with radius, for the luminous matter only. Four different models are plotted. The initial relaxed system is plotted as a solid line. As mentioned above, although initially isotropic, after relaxation the inner parts of the system develop some radial anisotropy. Dotted-dashed lines show different end results of our simulations. All refer to models with
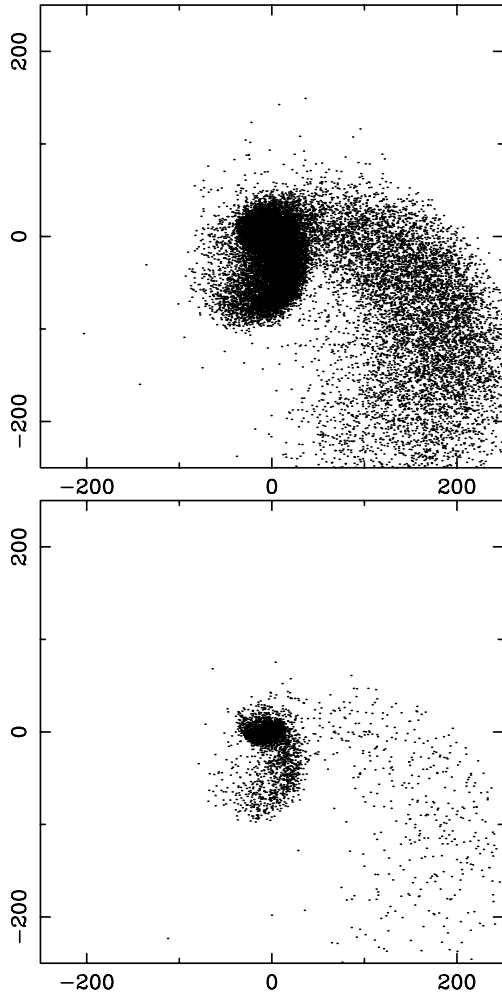
Figure 9. Luminous particles from the small system in run 2*o*. Many particles of this galaxy end up as shells in the merger remnant.

Figure 8. Particle distributions for halo (top) and luminous (bottom) components for run 4*g* as seen along the *z*-axis. The initial configuration of this run has a parabolic orbit with a fairly large impact parameter. Several tails in both components can be seen. Tails are mainly coming from the system with smallest mass. In the inner parts prominent shells can be seen (not visible in this plot). All particles in the tails will eventually fall back to the inner regions since they do not have enough energy to escape.

Figure 10. Radial velocity versus radius diagrams (V_r versus R) for the luminous particles of the smaller system for runs 2*o* (left panel) and 4*h* (right panel). The bands correspond to shells.

the same mass ratio but different orbital parameters. Up to a radius close to $R = 4R_e$ all systems are radially anisotropic (where R_e is the radius that includes half of the luminous mass in projection). For model 1*h*, with the largest impact parameter, the outer parts are close to isotropic. All merger remnants are more radially anisotropic than our initial relaxed system.

Merger remnants without halo resulting from head-on collisions also show radial anisotropy, while models with $D \neq 0$ show a trend that the tangential anisotropy of the remnants increases with increasing impact parameter. The fact that this trend is not clear in the present sample is probably related to the radial anisotropy that the initial system develops and to the effect of the halo in absorbing a significant fraction of the angular momentum.

4 DISCUSSION

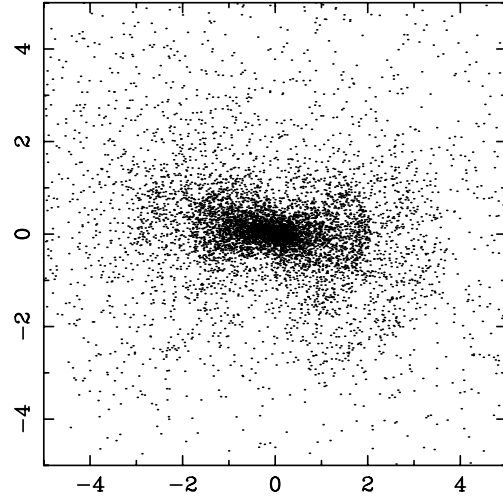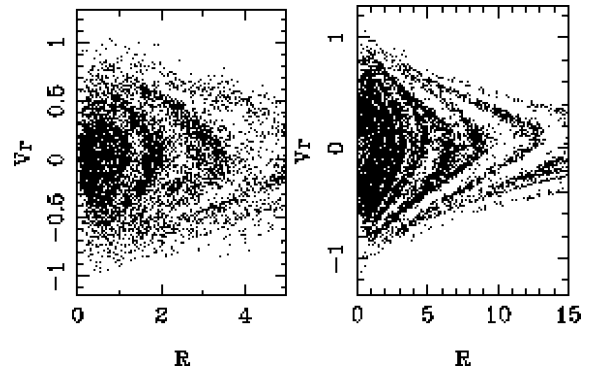We have carried out simulations of collisions between two-component realizations of elliptical galaxies consisting of a luminous and a dark halo component. The initial parameters are chosen such that all simulations end up in mergers.

The luminous parts of the merger remnants show a tendency to be prolate or triaxial, regardless of the initial angular momentum content of the orbit. This appears to be the case, because at the final stages prior to merger the systems encounter each other in nearly rectilinear orbits. Apparently, most of the orbital angular momentum is absorbed by the halo particles. Most of the luminous particles have radial orbits, giving the final cigar-shape figure. Since we start with spherical systems, it comes as no surprise that the remnants are closest to a sphere when the masses of the initial systems are dissimilar, as is also the case for models without halo.

This prolate to triaxial general shape is in agreement with claims by Ryden (1996), although Lambas, Maddox & Loveday (1992) argue that a triaxial shape is more consistent with the observed ellipticities in elliptical galaxies. Alam & Ryden (2002) find from the SLOAN digital sky survey that they can rule out with 99 per cent confidence that elliptical galaxies are oblate spheroids. Vincent & Ryden (2005) exclude with a 99 per cent confidence level that de Vaucouleurs galaxies from SLOAN Data Release 3 are oblate systems with equal triaxiality parameter for all isophotes. Bak & Slater (2000) on the contrary find a bimodal distribution with oblate and prolate spheroids.

Table 4. Morphological classification of the end products. The classification (column (2)) is indicative only; it refers to the value of the median when measuring the type from 100 random points of view. Columns (3) and (4) give a morphological description of each component.

| Model (1)	Hubble type (2)	Halo (3)	Luminous (4)
1*h*	E4−E5	Double lobe	Prolate, no rotation
1*o*	E4	Symmetrical tail	Two tails, prolate – triaxial, no rotation
1*g*	E4−E5	Prominent double tail	Triaxial, small rotation
2*h*	E5	Double asymmetrical lobe	Prolate + plume
2*o*	E3−E4	Single tail	Nearly triaxial
2*g*	E3−E4	Double asymmetric tail	Triaxial, rotation
4*h*	E3−E4	Single lobe	Prolate, shells
4*o*	E3	Several tails	Tails + shells
4*g*	E3	Several tails	Tails + shells (prom), rotation
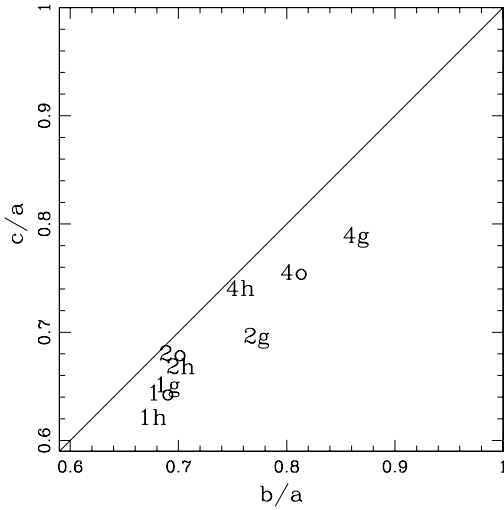
Figure 11. Following de Zeeuw & Franx (1991), we have plotted the axis ratios of our merger remnants in b/a, c/a space. Systems on the diagonal line are prolate, those on the line $b/a = 1$ are oblate.
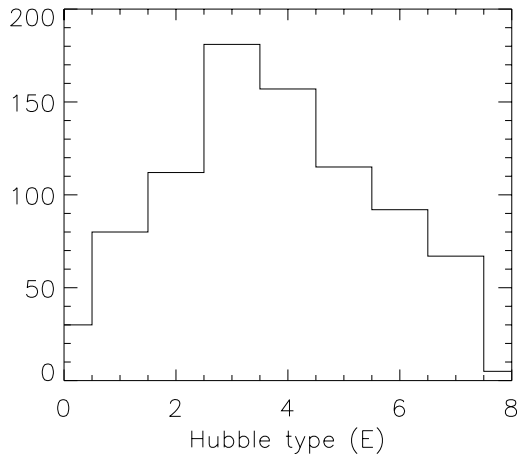

Figure 12. Histogram of Hubble types resulting from the merger simulations (all runs) by looking at the remnants from 100 random points of view.

Our systems show a peak in their Hubble-type distribution near E3. The sample is by no means complete. However, all remnants show the tendency to be prolate or triaxial and this result seems robust. Lambas et al. (1992) show that an E3 Hubble type is favoured.
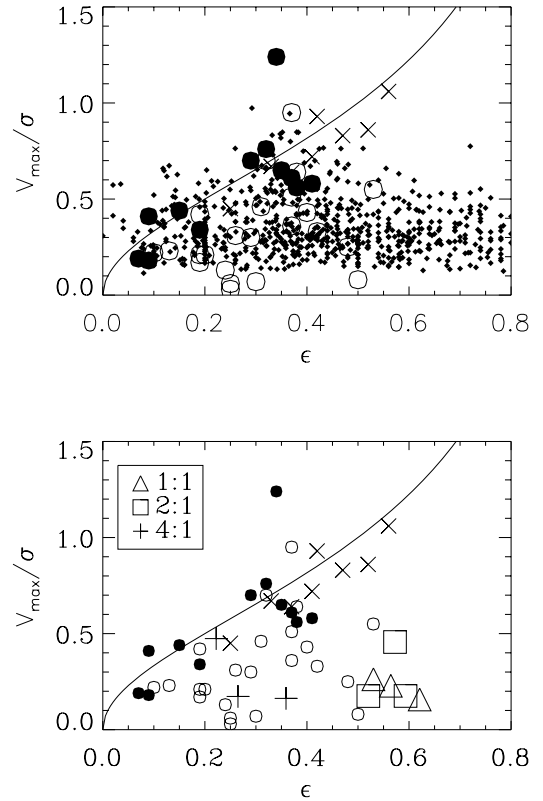

Figure 13. $V_{\max}/\sigma$ versus ellipticity diagram. In both panels observational data from Davies et al. (1983) are plotted: open circles are high-luminosity ellipticals, filled circles are low-luminosity ellipticals and crosses are bulges. The upper panel gives the cloud of points obtained when looking at each model from 100 points of view (small dots). The lower panel represents the models when seen from a point of view along the y-axis. Different symbols refer to the various mass-ratios used (see inset). Compare with fig. 11 in Paper I.

Similarly, Franx, Illingworth & de Zeeuw (1991) find that there is a peak around E3 in real elliptical galaxies. The situation is less clear in models without halo. In Paper I, we stressed that our results with regard to the final morphology must be put in the framework of the likelihood of having the specific initial conditions that we used.

Our remnants from systems with halo show low rotation. In general our merger remnants are non-rotating. This is also found in Paper I for head-on collisions. But here it is true for head-on as well as non-head-on collisions. For the encounters involving a
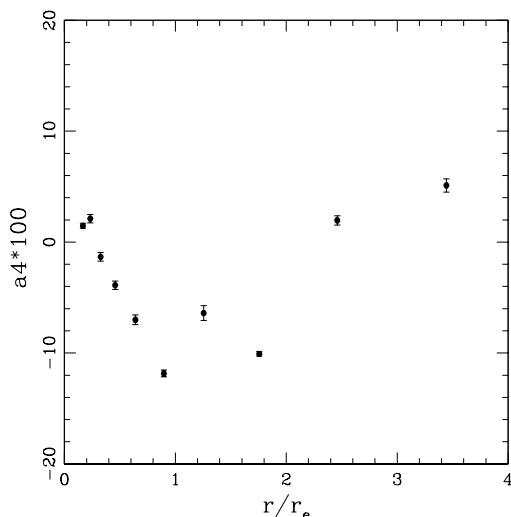
Figure 14. Mean radial variation of a_4 after equilibrium has been reached for model 1g. Negative a_4 indicates boxy isophotes.
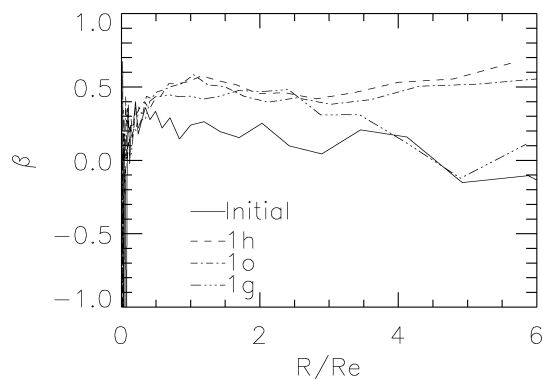

Figure 15. Anisotropy parameter versus radius. Positive values indicate radial anisotropy, negative ones indicate tangential anisotropy.

non-zero angular momentum in models without halo (Paper I), we found that the orbital angular momentum is transfered to spin angular momentum. For the present two-component models this is also true. However, now it is the halo that retains the spin angular momentum. As a result, this leaves the particles in the luminous bulges in radial orbits right before the final encounter leading to the merger. This final encounter is a nearly head-on collision, no transfer of angular momentum to the bulges takes place, and the final system takes a nearly prolate shape.

This final encounter, almost head-on, is also responsible for the radial anisotropy found in the inner parts of the merger remnants in most of our simulations. The outer parts of the remnants from the simulations with large orbital angular momentum gain a small amount of rotation and are close to isotropic. In general, this would be in good agreement with data for high-luminosity elliptical galaxies. Therefore, we might propose mergers between spheroids with a halo as a possible origin for those systems.

Although the amount of dark matter in elliptical galaxies is still uncertain (Baes & Dejonghe 2001; Romanowsky et al. 2003), it

is of interest to look at the effect of dark matter on the properties of the merger remnants and the merging process in general. We can therefore compare the two samples, the one presented here and the one described in Paper I in a more general sense.

Head-on collisions for equal mass mergers show a very similar behaviour in both samples. The final systems are prolate, non-rotating radially anisotropic spheroids. Equal mass mergers with $D \neq 0$ show some differences. Non-halo models result in rotating spheroids supported by tangential anisotropy and may develop a bar or discy isophotes depending on the mass ratio of the progenitors. Halo models produce nearly prolate, radially anisotropic spheroids, mainly with boxy isophotes.

In this regard, we could trace the differences in shape and anisotropy observed in real elliptical galaxies to different formation mechanisms and contents of dark matter.

The results from Saglia et al. (1993) show that there might be two different populations of elliptical galaxies with regard to their dark matter halo. While elliptical galaxies with a dark halo show boxy deviations in their isophotes, galaxies that show no evidence for dark matter tend to be more discy. This difference may tell us something about different formation mechanisms.

The simulations in Paper I refer to mergers of spheroids without a dark matter halo. This situation may apply to spherical systems surrounded by the global potential well of a cluster. Two cases may apply here. Elliptical galaxies in the central region of the cluster may have lost their halo, which is now a part of the cluster halo. Another possibility is that the global potential well of the cluster dominates. The case *with* dark matter haloes would seem to be more relevant for elliptical galaxies in the field.

High-resolution cosmological *N*-body simulations produce cluster halos containing many 'subhaloes' which are plausibly identified as the dark haloes of individual galaxies (Klypin et al. 1999; Moore et al. 1999). These haloes, although truncated, may still be massive and extended enough to play a dynamical role in E+E mergers, blurring somehow the above scheme.

Such a scheme could in principle be easily tested with observations given the differences in morphology and kinematics observed in our two samples. But the possibility that elliptical galaxies can be built out of mergers of discs introduces a complication.

Based on the simulations described above, and according to the scheme presented, we can propose a formation mechanism for these two different populations of elliptical galaxies. Those with signatures of a dark matter halo might be formed by a merger of two spheroidal systems surrounded by a halo, probably in the field or in compact groups (Kelm & Focardi 2004). The remnant would show preferentially boxy deviations. Those without a clear signature of a halo might be formed inside a cluster and the formation mechanism followed would be that described by the models in Paper I, with a broad range of different characteristics and where some of them have discy deviations in their isophotes. In other words, we could expect some habitat segregation but opposite to the one reported by Shioya & Taniguchi (1993). This calls for further observational work.

Given the large range in properties of the merger remnants in our simulations, we may conclude that the formation of elliptical galaxies (at least for the high-luminosity ones) can in principle be explained by mergers of systems dominated by spheroidal components.

REFERENCES

Alam S. M. K., Ryden B. S., 2002, ApJ, 570, 610
Baes M., Dejonghe H., 2001, ApJ, 563, 19
Bak J., Slater T. S., 2000, AJ, 120, 110
Barnes J. E., 1998, in Friedli D., Martinet L., Pfenniger D., eds, Galaxies: Interactions and Star Formation. Saa-Fee Advanced Course 26. Springer-Verlag, Berlin/Heidelberg
Binney J., Tremaine S., 1987, Galactic Dynamics. Princeton Univ. Press
Binney J., Merrifield M., 1998, Galactic Astronomy. Princeton Univ. Press, Princeton NJ
Dantas C. C., Capelato H. V., Ribeiro A. L. B., de Carvalho R. R., 2003, MNRAS, 340, 398
Davies R. L., Efstathiou G., Fall S. M., Illinwort G., Schechter P. L., 1983, ApJ, 266, 41
Dehnen W., 1993, MNRAS, 265, 250
de Zeeuw T., Franx M., 1991, ARA&A, 29, 239
Franx M., Illingworth G., de Zeeuw T., 1991, ApJ, 383, 112
Fish R. A., 1964, ApJ, 139, 284
González-García A. C., 2003, PhD thesis, Univ. of Groningen
González-García A. C., van Albada T. S. 2005, MNRAS, in press (this issue: doi 10.1111/j.1365-2966.2005.09242) (Paper I)
Hernquist L., 1987, ApJS, 64, 715
Hernquist L., 1990a, ApJ, 356, 359
Hernquist L., 1990b, J. Comp. Phys., 87, 137
Jaffe W., 1983, MNRAS, 202, 995
Jørgensen I., Franx M., Kjærgaard P., 1996, MNRAS, 280, 167
Keeton C. R., Kochanek C. S., Falco E. E., 1998, ApJ, 509, 561
Kelm B., Focardi P., 2004, A&A, 418, 937
Klypin A., Kravtsov A., Valenzuela O., Prada F., 1999, ApJ, 522, 82
Kronawitter A., Saglia R. P., Gerhard O., Bender R., 2000, A&AS, 144, 53
Lambas D. G., Maddox S. J., Loveday J., 1992, MNRAS, 258, 404
Matsushita K., Makishima K., Ikebe Y., Rokutanda E., Yamasaki N., Ohashi T., 1998, ApJ, 499, 13
Moore B., Ghigna S., Governato F., Lake G., Quinn T., Stadel J., Tozzi P., 1999, ApJ, 524, 19
Napolitano N. R. et al., 2005, MNRAS, 357, 691
Renzini A., Ciotti L., 1993, ApJ, 416, L49
Romanowsky A. J., Douglas N. G., Kuijken K., Merrifield M. R., Arnaboldi M., Freeman K. C., Taylor K., 2001, AAS, 19915303R
Romanowsky A. J., Douglas N. G., Arnaboldi M., Kuijken K., Merrifield M. R., Napolitano N., Capaccioli M., Freeman K. C., 2003, Sci, 301, 1696
Ryden B., 1996, ApJ, 461, 146
Saglia R. P., Bertin G., Stiavelli M., 1992, ApJ, 384, 433
Saglia R. P., Bender R., Dressler A., 1993, A&A, 279, 75
Shioya Y., Taniguchi Y., 1993, PASJ, 45, L39
Smulders M., Balcells M., 1995, Master thesis Project, Univ. of Groningen
Vincent R. A., Ryden B. S., 2005, ApJ, 623, 137

This paper has been typeset from a TEX/LATEX file prepared by the author.